Journal Pre-proof

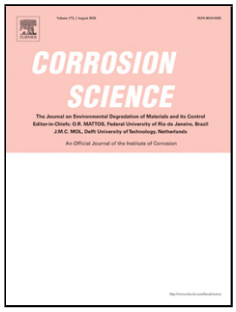

The ability of Mg_2Ge crystals to behave as 'smart release' inhibitors of the aqueous corrosion of Zn-Al-Mg alloys

N. Wint (Validation) (Formal analysis) (Investigation) (Data curation)<ce:contributor-role>Writing - original and draft)<ce:contributor-role>Writing- review and editing), A.D. Malla (Investigation) (Data curation), N. Cooze (Investigation) (Data curation), T. Savill (Investigation) (Data curation), S. Mehraban (Investigation) (Data curation) (Methodology), T. Dunlop (Investigation) (Data curation), J.H. Sullivan (Conceptualization) (Methodology) (Validation) (Formal analysis) (Investigation) (Data curation)<ce:contributor-role>Writing - original and draft)<ce:contributor-role>Writing- review and editing), D. Penney (Conceptualization) (Methodology) (Validation) (Formal analysis) (Investigation), G. Williams (Conceptualization) (Methodology) (Writing - review and editing) (Supervision), H.N. McMurray (Conceptualization) (Methodology) (Writing - review and editing) (Supervision)

PII: S0010-938X(20)32372-6

DOI: https://doi.org/10.1016/j.corsci.2020.109091

Reference: CS 109091

To appear in: *Corrosion Science*

Received Date: 22 February 2020

Revised Date: 20 October 2020

Accepted Date: 28 October 2020

Please cite this article as: Wint N, Malla AD, Cooze N, Savill T, Mehraban S, Dunlop T, Sullivan JH, Penney D, Williams G, McMurray HN, The ability of Mg_2Ge crystals to behave as 'smart release' inhibitors of the aqueous corrosion of Zn-Al-Mg alloys, *Corrosion Science*

(2020), doi: https://doi.org/10.1016/j.corsci.2020.109091

The ability of Mg_2Ge crystals to behave as 'smart release' inhibitors of the aqueous corrosion of Zn-Al-Mg alloys.

N. Wint * A. D. Malla, N. Cooze, T. Savill, S. Mehraban, T. Dunlop, J. H. Sullivan, D. Penney, G. Williams, H. N. McMurray

Materials Research Centre, College of Engineering, Swansea University, Bay Campus, Fabian Way, Crymlyn Burrow, Swansea, UK, SA1 8EN

*Corresponding author:
E-mail address: n.wint@swansea.ac.uk

Highlights

- Additions of up to1.8 wt. % Ge in Zn-1.6 wt. % Al-1.6 wt. % Mg.
- SVET and time lapse microscopy study of Zn-Al-Mg-Ge corroding in NaCl.
- Ge additions result in formation of new Mg_2Ge phase within the microstrusture.
- Reduction in SVET derived mass loss and corroded area with increasing Ge levels.
- Dissolving Mg_2Ge acts as source of Mg^{2+} resulting in stabilisation of Zn surface.

Abstract:

In-situ scanning vibrating electrode technique and time-lapse microscopy are used to investigate the influence of germanium additions (0.19-1.8 wt.%) on the corrosion performance of zinc-aluminium-magnesium model alloys immersed in 0.17 $mol.dm^{-3}$ NaCl. The addition of Ge results in the formation of Mg_2Ge and a decrease in the fractional area of eutectic phase. A 58 % decrease in SVET derived mass loss is achieved at 1.8 wt.% Ge. It is proposed that Mg_2Ge crystals are anodically attacked and behave as reservoirs of Mg^{2+} ions. $Mg(OH)_2$ is precipitated and local electrolyte pH stabilises to values at which the zinc surface is passive.

Keywords: A Alloy A Metal Coating A Zinc A Aluminium A Magnesium C De alloying

1. Introduction

Zinc and zinc based alloy coatings are able to provide sacrificial protection to underlying steel substrates and are heavily utilised within the automotive and construction industries. Despite the superior corrosion properties afforded by zinc coatings, there is a growing demand to both improve coating performance, and to lower coating weights. One approach is to introduce alloying additions into galvanized zinc coatings, and the kinetics and mechanism of zinc alloy corrosion has been investigated extensively in a range of environments. [1-24] Active inhibition can also be provided by corrosion inhibitors, which are released from the organic coating matrix upon exposure to stimuli (for example contact with a corrosive electrolyte). [25-26] Active corrosion inhibitors are primarily added to organic components of an organic coating system (e.g. pre-treatment, primer, topcoat) and their incorporation into metallic coatings is, to date, limited. The aim of this paper is therefore to investigate the ability of Mg_2Ge crystals, formed within metallic Zn-Al-Mg (ZAM) alloys, to behave as corrosion inhibitors and provide active corrosion protection.

The effect of alloying additions on the corrosion rate of ZAM alloys has been extensively researched. [1-24] The $MgZn_2$ and $MgZn_{11}$ intermetallic particles, formed in zinc-magnesium and ZAM alloys, have been shown to undergo preferential anodic attack. [5, 12, 22] and the

magnesium oxide formed can locally replace zinc oxide. [5, 12, 22] Magnesium oxide is a wide band gap (~ 7 eV) semiconductor (effectively an insulator by comparison to zinc oxide (~ 3 eV), [27] and has been shown reduce rates of the cathodic oxygen reduction reaction (ORR). [8, 12] Mg^{2+} ions, released during anodic dissolution of intermetallic particles, can also react with OH^- (formed at the cathode) to form magnesium hydroxide ($Mg(OH)_2$) which has the effect of 'buffering' surface pH to mildly alkaline values (~pH 10.2) [1]. At these vales of pH protective zinc hydr(oxides) and simonkolleite are stable [2, 7] but aluminium, present within ZAM, is predicted to become anodically active. Anodic dissolution of aluminium produces aluminates which can react with Mg^{2+} to form protective layered double hydroxides (LDH).[2, 7 16]

Other alloying elements under investigation include Ge, [28] and the addition of 0.3-0.5 wt.% Ge to industrially relevant Mg-1 wt.% Zn binary alloys [29] has led to the formation of 'inert' Mg_2Ge intermetallic particles [30] which are cathodically polarised during OCP and potentiondynamic polarisation exposure of Mg alloys. [29]

In comparison, active corrosion inhibition is typically achieved by the direct incorporation of inhibitive pigments into an organic coating. However, interaction between inhibitors and the surrounding matrix can lead to loss of inhibition capability, reduced lifespan and complete organic coating failure. As well as effectively inhibiting corrosion, inhibitive pigments must be able to leach (release and transport) to defective areas, where they can form protective layers. [31] The use of low solubility pigments, which are unable to release and transport to coatings defects, can result in incomplete coating inhibition. High solubility pigments can rapidly leach out of the organic coating and cause osmotic blistering. [26, 32-36] In recent years, significant effort has instead been focused on the development of 'self-healing' organic coatings, whereby a protective corrosion inhibitor is

encapsulated by 'nano-containers' so that matrix-inhibitor interaction cannot occur. The containers are evenly distributed throughout the coating and the controlled release of the inhibitive pigment is instead triggered by external mechanical (e.g. coating abrasion or cracking) or chemical (e.g. pH) stimuli. [25-26] To date, several attempts at nano-container design have been made. These include: polymer based capsules, [39] halloysites (aluminosilicates), [40-42] polyelectrolyte shells, [43] layered double hydroxides (LDH), [44] ion exchange resins, [45] conducing polymers, [46] and mesoporous inorganic materials (e.g. silica) [41, 47]. Other factors to consider are the control of the capsule permeability by variations in external stimuli (for example pH, temperature, ionic strength etc), as well as container size. [25-26] Nano-containers should be less than 300-400 nm in size to avoid the creation of hollow cavities and risk to coating integrity.[26]

To date the majority of research into the use of nano-containers is focused on their inclusion into organic coatings as opposed to metallic coatings. [54] More recently, inorganic nano-containers such as halloysites and mesoporous silicon have become the topic of increasing research. [47-56] Both types of nano-container are commercially available in large quantities and are more economically feasible than alternatives. [57] They also offer the additional potential benefits of mechanical and thermal stability [40, 42] which means that it is possible for them to be incorporated into metallic coating systems. However, in order to embed these nano-capsules in metallic coatings, it is necessary to functionalize their surfaces and much of the published work in this area focuses on the modification of nano-containers. [47-56] In order that these smart release vehicles provide adequate corrosion inhibition it is vital that the nano-containers are compatible with other components present in the metal matrix and both the zeta potential of particles, and their electrostatic interaction with the surface,

[48-53] have been identified as crucial factors which influence their incorporation into the matrix.

Given 1.) the ability to form Mg_2Ge intermetallic particles within zinc alloys, [30, 58] and 2.) the ability of Mg^{2+} ions (released during the dissolution of Mg based intermetallics) to reduce corrosion rates, [59-61] it seems plausible that the addition of Ge to ZAM alloys would result in the formation of thermally and mechanically stable, intermetallic 'smart release' capsules, and a reduction in ZAM corrosion rate.

This paper describes an investigation into the effect of Ge additions (0-1.8 wt.%) on the kinetics and mechanism of ZAM corrosion, as it occurs in 0.17 $mol.dm^{-3}$ NaCl. In so doing the amount of Ge, added to a ZAM (1.6 wt.% Al, 1.6 wt.% Mg) master alloy, is systematically changed and the resultant microstructure is characterised using SEM. The relative nobility of the phases present are determined using scanning Kelvin probe force microscopy (SKPFM). The scanning vibrating electrode technique (SVET) derived mass loss is used to assess the corrosion performance of ZAM-Ge alloys, and time lapse microscopy (TLM) is used to provide mechanistic information regarding the corrosion at a microstructural level. Complimentary open circuit measurements (OCP) measurements are also conducted.

2. Materials and Method

2.1 Materials

ZAM-Ge samples were produced in an inert (argon) environment. ZAM (96.8 wt.% Zn, 1.6 wt.% Mg and 1.6 wt.% of Al) pieces, obtained from Tata Steel UK, were heated to 650^{o}C in a crucible. Varying amounts of Ge were added to produce four different alloy compositions and the mixture was further heated to 1000^{o}C. Samples were then air cooled

within the crucible. A IR thermometer optris CT laser 3M pyrometer was used to measure the temperature on the alloy surface.

Chemicals including nitric acid (HNO_3), ethanol (C_2H_5OH), hydrochloric acid (HCl), sodium hydroxide (NaOH) and phenolphthalein ($C_{20}H_{14}O_4$) were supplied by Sigma-Aldrich Chemical Co. and were of analytical grade purity. A 0.17 $mol.dm^{-3}$ NaCl electrolyte was used throughout. Bulk solution pH was adjusted by the drop-wise addition of either HCl (aq) or NaOH (aq).

2.2 Methods

Microstructural analysis; The ZAM-Ge samples were mounted in Conducto-Mount (Metprep Ltd) conductive phenolic resin, ground to a European P grade P2400 grit finish using abrasive silicon carbide (SiC) paper and then polished with a 1 µm diamond slurry. The polished samples were etched using 3 wt.% Nital and rinsed with water and ethanol. Images of each of the alloy microstructure were obtained using a Hitachi TM3000 Scanning Electron Microscope (SEM) with a Bruker Energy Dispersive X-ray Spectroscopy (EDS) module. The volume fraction of each of the different microstructural phases was determined by image analysis of five SEM images. A Bruker D8 Discover X-ray Diffractometer (XRD) was used to identify the crystal phases present within the alloy. The XRD apparatus consited of a copper point source (40 kV and 40 mA) used in conjunction with a poly-capillary element and a 2 mm collimator. The step size was 0.025 degrees and the step time was 0.5 seconds. X-rays were detected using a 1D LYNXEYE detector with a 2.26 degree opening.

SKPFM; The potential difference between phases present within the ZAM-Ge alloys were investigated using a JPK NanoWizard3 atomic-force microscope (AFM) with scanning

Kelvin probe (SKP) equipped with a FM-50 193Pointprobe® tip. The measurements were taken in AC (tapping) mode and performed at a distance of 20 nm from the sample surface at 20 μm/s speeds. Samples were prepared in the same way as those used for TLM.

Time lapse microscopy; Samples were mounted in a non-conductive phenolic resin and prepared in the same way as those used for SEM and XRD analysis. 3M non-conductive polytetrafluoroethylene (PTFE) tape was used to expose a 0.78 mm^2 circular sample area of the mounted sample before it was securely attached to the base of the petri dish. A Meiji Techno 7100 optical microscope, in conjunction with an Infinity 2 digital camera attachment, was used to acquire images following a methodology described in detail previously.[4, 19] A shroud was placed over the microscope objective lens which was manoeuvred into a position which allowed for the alloy microstructure to be imaged. [4, 19] The sample was immersed in 250 ml of electrolyte. An image was taken every two minutes for up to 24 hours. A 36 second time-lapse video was produced using Microsoft Movie Maker and 1 second of the video therefore corresponds to 40 minutes of image acquisition.

Scanning Vibrating Electrode Technique (SVET); SVET can be used to monitor the corrosion behaviour of a material, immersed within an aqueous electrolyte, with both spatial and temporal resolution.

The SVET instrumentation design, operating procedure, and the calibration process necessary to calculate the current flux density along the axis of probe vibration (j_z), have been described in detail previously. [62-67] A glass enclosed platinum wire micro-tip probe (125 μm diameter) is vibrated in the *z* direction above an immersed sample at a constant frequency (140 Hz), amplitude (25 μm) and height (100 μm). During the corrosion process ionic current flows between the anodic and cathodic region of the immersed sample. [62-67]

The SVET probe is able to detect an alternating potential at the frequency at which it vibrates. This alternating potential is proportional to the potential gradient (in the direction of vibration) established by the ionic current flux.

Samples were prepared in the same way as those used for TLM with the exception that a larger square area of 6 mm x 6 mm was exposed to the electrolyte. 60 measurements were made in both the *x* (width) and *y* (length) direction, thus creating a mesh of 3600 data points. Measurements were taken at 1 hour intervals over a total experimental time period of 24 hours and three experiments were conducted on each different alloy type. The concentration of dissolved oxygen and carbon dioxide, present within the electrolyte, were assumed to be the equilibrium concentration values for air saturated water (2.8×10^{-4} mol. dm^{-3} and 1.32×10^{-5} mol. dm^{-3} respectively). [68]

The time dependent total anodic current ($I(t)$), associated with each of the j_z distribution maps, can be obtained via Equation 1 by numerical integration of all the anodic (positive) $j_z(x, y)$ values recorded. [62, 69]

$$I(t) = A.J(t) = \int_0^X \int_0^Y [\, j_z(x, y, t) > 0] \, \mathrm{d}x \, \mathrm{d}y \tag{1}$$

A is the sample area, *X* and *Y* are the length and width of the area scanned and *t* is the time. Dividing *I(t)* by *A* allows for the determination of an area averaged anodic current density value *J(t)*.

The total charge density emitted over the duration of the experiment can be calculated using Equation 2 and the mass loss calculated using Faraday's law [62]

$$q = \frac{2Fm}{M} = \int_{t=0}^{t=t_{max}} j(t) \mathrm{d}t \tag{2}$$

where q is the total charge density, m is the mass loss per unit area, M is the atomic weight of zinc (65.38 Da), n is the valence of metal ions (2 in the case of Zn), F is the Faraday constant and t_{max} is the total immersion time. It is assumed that $j(t)$ remains constant between scans.

SVET is only able to resolve localized corrosion separated by distances greater than the scan height (in this case 100 µm). For cases that $h \gg$ the separation distance, the anodic current flux lines associated with the local feature will tend to pass under the plane of scan. [62, 69-70] The values of mass loss obtained using Faraday's Law will therefore only approach the true value in cases that $h \ll$ the separation distance, and anodic current flux cuts the plane of scan in an approximately normal fashion. The theoretical width at half maximum (*whm*) of the SVET response peak is $1.53h$ for a current point source. [66] The finite width of the electrically sensitive portion of the SVET probe results in peak broadening, and the *whm* of the SVET used during this work is actually $2.60h$ (260 µm in the case that $h = 100\ \mu m$). [65]

Although there are several limitations associated with the SVET technique, mass loss values calculated using Equation 2 have been shown to compare well with those obtained from external weather Zn run off tests. [71] Hydrogen gas evolution rates, obtained from area averaged cathodic current data, have also been shown to be comparable to those obtained when measuring H_2 evolution volumetrically. [70] Elsewhere, a strong correlation has been observed between SVET derived corrosion inhibition efficiency values and those calculated using EIS, gravimetric mass loss and polarization data. [72]

Electrochemical Measurements; Samples were ground to a European P grade P1200 finish using abrasive SiC paper. The sample was washed using deionised water and ethanol. A

0.78 mm^2 area was exposed to 250 ml of electrolyte. The measurements were carried out using a Solatron 1280 potentiostat and all potential values were measured with respect to a standard calomel electrode (SCE).

Linear polarisation resistance measurements were carried out on ZAM-0 Ge and ZAM-1.8 Ge where the samples were polarised by 15 mV at a scan rate of 0.166 mVs^{-1}. This was carried out for both samples after 10 mins immersion in 0.17 $mol.dm^{-3}$ NaCl pH 7 and subsequently every hour for 5 hours.

3. Results

3.1 Materials Characterisation

The composition of the alloys under investigation are presented in Table 1.

(Table 1)

The SEM image of an industrially produced Zn-1.6 wt.%Al-1.6 wt.% Mg coating is shown in Figure 1. The coating is composed of three different phases; primary zinc dendrites (~30-50 µm) binary eutectic and ternary eutectic. Binary phases are lamellar structures made up of primary zinc and $MgZn_2$, whilst the ternary eutectic consists of primary zinc, $MgZn_2$ and aluminium nodules. SEM images of the four different ZAM-Ge cast microstructures are shown in Figure 2. The ZAM-0 Ge microstructure is comparable to that observed in Figure 1 for the industial ZAM coating.

(Figure 1)

(Figure 2)

The average area fraction of each phase, calculated from 5 different areas of each type of alloy, are shown in Table 2. The composition of each phase present is shown in Table 3.

(Table 2)

(Table 3)

The ZAM-0 Ge microstructure (Figure 2a) is composed of primary Zn rich dendrites along with binary and ternary eutectic, in line with the phases observed in the industrially produced coating shown in Figure 1. The addition of Ge into the ZAM alloy system results in the formation of a new phase within the microstrusture. XRD analysis (Figure 3) confirms that the phase formed is magnesium germanide (Mg_2Ge) which has been shown to form previously in magnesium [30] and ZAM alloys [58] which contain Ge additions. This phase can be seen to exist in two different forms. For all Ge containing samples a Mg_2Ge plate-like structure is present. As the wt.% Ge additions are increased faceted Mg_2Ge crystals are observed in the microstructure in addition to these 'plates'. At the highest concentration, ZAM-1.8 Ge (Figure 2d), large Mg_2Ge crystals are observed in the microstructure that demonstrate a 'Hopper' crystal morphology. The percentage of the surface area covered by Mg_2Ge increases from 1.6 % in the ZAM-0.19 Ge sample to 14.3 % in ZAM-1.8 Ge sample. The Mg containing eutectic phase decreases correspondingly, from 32.3 % to 7.4 %. Additionally, the surface area fraction of primary Zn increases from 67.5 % for ZAM-0 Ge to 78.3 % for ZAM-1.8 Ge. Examination of the microstructural morphology indicates that the Mg_2Ge crystals and plates are encased within the primary Zn phase suggesting that they are the first phase to solidify during freezing and provide subsequent nucleation sites for the primary Zn.

(Figure 3)

3.2 Electrochemical Measurements

Figure 4 shows the OCP of the various ZAM-Ge samples immersed in pH 7 0.17 mol.dm^{-3} NaCl over a 24 hour time period. In all cases the initial potential is ~ -1.02 V vs. SCE afterwhich a decrease in potential is observed in the first hour of the experiment. The initial drop in potential is dependent upon Ge content. For ZAM-0 Ge there is a small initial drop in OCP to ~ -1.03 V vs SCE. The OCP values then vary between -1.02 and -1.04V vs SCE over the 24 hour experiment. For ZAM-0.19 Ge and ZAM-0.87 the potential falls to ~ -1.04 V vs. SCE and ~ -1.06 V vs. SCE respectively. However, in the case of ZAM-1.8 Ge the potential decreases to ~ -1.14 V vs. SCE afterwhich it gradually increases and reaches -1.05 V vs. SCE after a 6 hour time period. The potentials for all the alloys converge towards ~ -1.04V ± 0.01V vs SCE after 24 hours.

(Figure 4)

In order to ascertain the difference in corrosion behaviour during the initial hours linear polarisation measurements were performed on samples of ZAM-0 Ge and ZAM 1-8 Ge for 5 hours with measurements made after 10 mins and subsequently after each hour. The polarisation resistances are given in Table 4.

(Table 4)

The R_p values for ZAM-1.8 Ge are around one order of magnitude greater than those of ZAM-0 Ge throughout the 5 hours indicating a consistently lower corrosion current as $i_{corr} \propto 1/R_p$.

3.3 SKPFM Results

A Volta potential difference map of an area of the ZAM-0.87 Ge surface is shown in figure 5. The different Volta potential difference values shown correlate well with the microstructural features observed in the SEM images (Figure 2). The more noble areas of the microstructure correspond to the zinc rich regions associated with the primary zinc dendrites and zinc lamellae within the eutectic structure. The $MgZn_2$ lamellae within the eutectic have more active potentials and this supports previous findings that this phase undergoes preferential corrosion in ZAM-0 Ge alloys. [19] The Mg_2Ge crystal is also associated with a more negative value (more active) with respect to the zinc dendrites anodic attack of the crystals is, thermodynamically, more likely to occur. The potential values shown have been rebased such that 0 mV corresponds to the highest potential and the values observed should not be used quantitively but rather in terms of relative nobility. Although an approximately linear relationship has been found to exist between Volta (contact) potential and electrochemical potential [73-74], more recently it has been shown that a reverse effect may exist between Volta potential differences (as obtained using SKPFM) and corrosion behavior for both iron/niobium couples, and nickel aluminum bronzes [75-76] In the former work the authors compared the corrosion behavior of iron (which is active at low pH) and niobium (which is active in alkali conditions). [75]They showed that for niobium the corrosion potential values measured during immersion conditions correlate well with Volta measurements correlated well across the whole pH range. [75] This was not true for iron meaning that the Volta potential differences obtained at both pH 4 and pH 7 wrongly predicted niobium to be the more active material. [75] It was concluded that the composition, microstructure and environment should all be taken into consideration, and that the existence of a correlation. between corrosion behavior and Volta potential differences should be checked for all new systems. In this work, the results shown in Figure 5 would tend to suggest that the Mg_2Ge will form the anode in a couple with primary zinc. The

correlation between Volta potential difference and corrosion behavior has been verified for a similar ZAM system, immersed in pH 7 0.17 mol.dm^{-3} NaCl, during a previous investigation and the interpretation of the Volta potential differences shown in Figure 5 is therefore believed to be accurate. This finding is especially pertinent to the alloy with highest Ge addition, ZAM-1.8 Ge, as the surface area fraction of eutectic and hence $MgZn_2$ is significantly reduced as compared to the ZAM-0 Ge alloy.

(Figure 5)

3.4 SVET

Figure 6 shows the normal current density measured above the surface of the various ZAM-Ge alloys freely corroding in pH 7 0.17 mol.dm^{-3} NaCl. In the case ZAM-0 Ge, corrosion is highly localized from the outset and the anode (red) positions remain somewhat fixed with time once initiated. Peak anodic current densities of approximately 5 A.m^{-2} are recorded. As the level of Ge additions increases the number of individual anodic features decreases. For ZAM-1.8 Ge the initiation of anodic attack is delayed for several hours and, once established, is more generalised in nature. Lower values of peak anodic current densities are observed. The relative SVET derived metal loss (calculated using Equation 2) from ZAM-Ge samples after 24 hours of immersion in 0.17 mold.dm^{-3} NaCl are shown in Table 5. Errors shown are based on the standard deviation of three measurements. The metal loss from ZAM-0.19 Ge is 8.53 g.m^{-2} compared to 5.01 g.m^{-2} recorded for ZAM-0 Ge. The values caculated for ZAM-0.87 Ge and ZAM-1.8 Ge were 4.41 g.m^{-2} and 2.11 g.m^{-2} resepctively. It therefore appears that the Ge additions can significalty reduce the metal loss in these alloys when added at levels above a threshold amount.

(Figure 6)

(Table 5)

3.5 Time lapse microscopy (TLM)

The corrosion resistance afforded by the ZAM-1.8 Ge can be further investigated using TLM which allows for the acquisition of information regarding the mechanism of corrosion on a microstructural level with respect to time. Figure 7 shows optical microscopy images of the surface of ZAM-Ge alloys after various times of immersion in pH 7 0.17 $mol.dm^{-3}$ NaCl. Two anodic features (labelled in Figure 7a) are obversed on the surface of ZAM-0 Ge after just 1 hour of immersion, afterwhich they increase in size (see also S1). A dark ring (also labelled), consistent with corrosion product formation, is visible at a distance from the anodes and becomes thicker with time. Corrosion product rings have previously been claimed to form at boundaries at which ionic counter currents (metal ions produced at the anode and hydroxide ions produced at the cathode) meet. [4] In the case of ZAM-1.8 Ge (Figure 7b) the appearance of similar corrosion features within the eutectic is delayed. However, darkening of the Mg_2Ge crystals was observed during this initial period. After 6 hours corrosion can be seen at the boundary between Mg_2Ge crystals and primary zinc and anodic features, similar to those seen in the ZAM-0 Ge material, develop. The anode-cathode spacing, as determined by the distance from the anode to the corrosion product ring, is considerably smaller (typically ~ 75 μm), than that observed on ZAM-0 Ge (typically ~ 250 μm) and corrosion is somewhat constrained. This delay in initiation is explicit in the TLM video shown (S2).

(Figure 7)

The time it took for corrosion to initiate within the eutectic of the ZAM-1.8 Ge varied for repeat experiments during which different areas of the alloy surface were exposed to the

eletrolyte. Figure 8 shows optical microscopy images of 3 different areas of the ZAM-1.8Ge alloy surface after various times of immersion in pH 7 0.17 mol.dm^{-3} NaCl. In the case of the first experiment shown, corrosion does don't initiate within the eutectic for 7 hours. In the case of the second and third (please note that the images are slightly pink due to the presence of phenolphthalein) sample corrosion initiates after 1 hour and 5 hours respectively. Upon inspection it was found that the time to initiation correlated with the fraction of the exposed surface area which was covered by Mg_2Ge crystals. In the case of the second experiment (for which corrosion initiated within eutectice after 1 hour) Mg_2Ge crystals corresponded to 6.3% of the total surface area. Furthermore the crystals were not evenly distributed and concentrated on one side of the area. In comparison, for experiment 1 (7 hours initiation time) and 3 (5 hours initiation time), the Mg_2Ge constituted 8.2 % and 7.1 % of the surface area respectively. Crystals also appeared to be more evenly distibuted across the surface.

(Figure 8)

It would seem reasonable that the principal microstructural component contributing to the corrosion resistance afforded by the ZAM-1.8 Ge are the Mg_2Ge crystals. The corrosion of single Mg_2Ge crystals was investigated by completing EDS analysis prior to and following immersion in pH 7 0.17 mol.dm^{-3} NaCl solution for 2 hours. Figure 9a shows an SEM image of an Mg_2Ge crystal prior to immersion in NaCl. The weight percentage of Mg calculated using EDS prior to immersion was 37.5±2 wt. %. The average weight of those same crystals has dropped to 20.2±1 wt.% after 2 hours of immersion. The confidence limits (error bars) given correspond to ± one standard deviation on the mean of four measurements.

(Figure 9)

The dissolution of Mg and its subsequent reaction with OH^- ions, would result in a change in local electrolyte pH and thus phase stability. This effect was investigated by dosing the NaCl electrolyte with 1 wt. % phenolphthalein, an indicator which is colourless at pH values below pH 8 and turns pink above pH 8. Figure 10 shows a TLM image of the ZAM-0 Ge surface after 4 minutes of immersion in pH 7 0.17 $mol.dm^{-3}$ NaCl electrolyte dosed with 1 wt.% phenolphthalein. Both the image and the video (S3) shows the establishment of a pH gradient with respect to anodic and cathodic sites (pH < 8 surrounding the anodic sites and pH > 8 surrounding the cathodic sites). A similar pH gradient has been observed previously during the study of ZAM coatings. [19]

Figure 11 show the TLM images of the ZAM-1.8 Ge surface obtained after various times of immersion in pH 7 0.17 $mol.dm^{-3}$ NaCl containing 1 wt. % phenolphthalein. Initially the electrolyte pH is below 8 across the entire sample. After 1 hour the colour turns pink across the sample surface indicating a pH value greater than 8 (Video S4). Finally, after 14 hours a pH gradient is established (Figure 11d) similar to that shown in Figure 10.

To assess the exact nature of the pH that developed over the surface 6 x 6 mm samples of ZAM-0 Ge and ZAM 1.8 Ge were prepared identically as for SVET experiments. A droplet of 0.17 M NaCl at pH 7 was then added to cover these areas and left for 1 hour. After this time universal indicator paper was applied to each droplet. Figure 12 shows that for ZAM-0 Ge a pH of 9-10 developed over a region of the exposed sample area similar to that observed in the TLM.

(Figure 10)

(Figure 11)

(Figure 12)

4. Discussion

Although the exact mechanism by which ZAM-Ge alloys are able to provide corrosion protection is yet to be fully discerned, it would seem reasonable to propose that the principal microstructural components responsible for the increased resistance ZAM- 1.8 Ge observed in this work, are the Mg_2Ge crystals. Once in contact with the corrosive electrolyte it is believed that Mg_2Ge undergoes preferential anodic de-alloying (Figure 5) by loss of Mg^{2+}, leaving behind a surface enriched in Ge (Figure 8). This rapid anodic dissolution corresponds to the initial drop in corrosion potential observed for all three Ge containing samples (Figure 4). The Mg^{2+} ions released during this process react with the OH^- (generated at the cathode) to form $Mg(OH)_2$. $Mg(OH)_2$ has a solubility product K_{sp} of 1.8×10^{-11} $mol^3.dm^{-9}$ [78] and production of a $Mg(OH)_2$ corrosion product will ensure that local electrolyte pH is maintained at ~10.5, at which pH the zinc surface is passive. [2, 7] This notion is reinforced by the pink appearance (pH>8) of the electrolyte above the ZAM-1.8 Ge sample in the presence of 1 wt. % phenolphthalein (Figure 10). Mg_2Ge crystals act as a direct source of Mg^{2+} ions. In comparison, both Zn^{2+} and Mg^{2+} are formed during the dissolution of the eutectic $MgZn_2$ which occurs during the corrosion of ZAM-0 Ge alloys. [2, 4, 8] The hydrolysis of Zn^{2+} metal cations will result in local acidification [79] and limit the increase in pH which occurs during Mg dissolution with regions of electrolyte surrounding the anodic features remaining below pH 8 as shown in Figure 9. Thus, the surface of the ZAM-0 Ge sample may not develop Zn passivation across the entire sample area in contrast to ZAM-1.8 Ge samples.

Following this initial dissolution process the potential gradually increases (Figure 4) and stabilises at ~-1.05 V vs. SCE after approximately 6 hours for ZAM-1.8 Ge. The chemical conditions created on the surface of the ZAM-1.8 Ge alloy seem to provide a transient level of protection to the zinc. The time for which this protection lasts is believed to be dependent on both the size and distribution of Mg_2Ge crystals exposed at the surface. In the case of well distributed crystals, which cover a larger percentage of the surface area, it is plausible that there is a more uniform elevation in electrolyte pH. In comparison for smaller crystals the increase in electrolyte pH is highly localized. The local breakdown in the passive layer will result int the dissolution of zinc within the eutectic, initiating firstly at boundaries with the Mg_2Ge crystals. However, the increased bulk electrolyte pH means that the zinc cations (produced at the anodes) are only required to travel a short distance before the solubility limit associated with $Zn(OH)_2$ is reached. This means that, once initiated, corrosion on ZAM-1.8 Ge is constrained compared to that on ZAM-0 Ge (Figure 7) as shown by the smaller radius of the corrosion product ring. Evidence of zinc dissolution in these regions is demonstrated in Figure 11d by the visual attack of the zinc phase in the TLM images, and the establishment of a pH <8 around this anodic region indicative of Zn^{2+} hydrolysis.

At this point a question arises as to why the initial Mg_2Ge dissolution is not visible on SVET derived false colour maps shown for ZAM-1.8 Ge in Figure 6. As illustrated by the SEM images in Figure 2, the average size of a Mg_2Ge crystal is ~ 100 µm which is below the instrumental *whm* of the SVET (~260 µm). [61]It is therefore seems likely that the SVET may not allow for the resolution of individual crystals due to their size. Additionally, the spacing between the dissolving Mg_2Ge crystals and cathodic regions in the primary zinc phase (anode to cathode spacing) may be less than the SVET tip scan height of 100 µm above the sample surface, and hence the lines of current flux between the anode and

cathode may not intersect the SVET plan of scan and therefore will not be detected. As such the reported metal loss in Table 3 is potentially an underestimate for the ZAM-1.8 Ge material as the SVET will only measure mass loss due to such localised corrosion where anodes and cathodes are separated by distances greater than the SVET tip scan height. In order to further interrogate the SVET data to show the effect of Ge additions on the corrosion behaviour the anodic current integrals for each hour, *I(t)*, were plotted for both ZAM-0 Ge and ZAM-1.8 Ge samples and the range of currents for each hour are shown in Figure 13. The displayed ranges represent the maximum and minimum localised anodic currents at each hour as measured by the SVET across three repeated experiments for each material.

Figure 13 shows that integrated localised anodic corrosion currents between 3.0 and 8.3 x 10^{-6} A were measured from the initial scan for ZAM-0 Ge. In contrast, lower levels of localised corrosion, < 1 x 10^{-6} A, were observed for ZAM-1.8 Ge samples in the initial hours consistent with the dissolution of Mg^{2+} from Mg_2Ge being below the detection resolution of the instrument as discussed previously. However, at time frames between 6 - 16 hours, coinciding with the visible initiation of corrosion in the Zn phase in the TLM and the rise in potential towards that of the ZAM-0 Ge in the OCP, localised corrosion is detected by the SVET and critically the maximum anodic current levels remain significantly lower than the minimum anodic currents of the ZAM-0 Ge. These lower levels of localised anodic current for ZAM-1.8 Ge are observed throughout the 24 hour experiment with only one incidence of the current ranges coinciding after 23 hours. This provides evidence that the levels of localised anodic activity are reduced for samples containing 1.8 wt% Ge additions.

The R_p values for ZAM-1.8 Ge are around one order of magnitude greater than those of ZAM-0 Ge throughout the 5 hours. These data therefore suggest that the during the release of Mg^{2+} from Mg_2Ge, the corrosion kinetics of the ZAM-1.8 Ge system are reduced in comparison to the corrosion of the ZAM-0 Ge.

The increase in potential (Figure 4) and anodic activity (Figure 6) observed for ZAM-1.8 Ge samples after 1-7 hours of immersion indicates that Mg_2Ge is only able to provide a transient inhibitive effect. Nevertheless, the introduction of Mg_2Ge into ZAM coatings, (and absence of $MgZn_2$ and Mg_2Zn_{11}) to provide enhanced corrosion protection is of interest, particularly for applications where electrolyte exposure is limited (for example in the case of organically coated systems in which ZAM is typically used), and is worthy of further investigation and optimisation.

5. Conclusions

A systematic study into the effect of Ge additions on the corrosion resistance afforded by Zn-Al-Mg alloy coatings has been completed to so show that;

- the addition of Ge into the ZAM alloy system resulted in the formation of a new Mg_2Ge phase within the microstrusture. This phase existed in two different forms. At all levels of Ge addition, a Mg_2Ge plate like structure was observed and at the highest concentration (ZAM-1.8 Ge) large Mg_2Ge crystals were also observed. The area fraction of the Mg containing eutectic phase decreased with increasing Ge content.

- Upon exposure to pH 7 0.17 $mol.dm^{-3}$ NaCl, Mg_2Ge undergoes preferential galvanic attack with anodic de-alloying and loss of Mg^{2+}, leaving behind a surface enriched in Ge. This galvanic attack causes a decrease in open circuit potential for

all ZAM-Ge samples over the initial hours of exposure. The shift to more negative potentials was larger at increased levels of Ge. The OCP rises to that of the ZAM-0 Ge sample over time as Mg is depleted from the Mg_2Ge crystals.

- The galvanic attack of the Mg_2Ge has a lower corrosion rate over the initial 5 hours than samples with 0 wt % Ge, for which localised corrosion of the alloy occurs immediately on exposure to the electrolyte.

- This initial galvanic attack of Mg_2Ge releases Mg^{2+} ions that react with the OH^- (generated at the cathode) to form $Mg(OH)_2$ enabling the electrolyte pH to reach pH 9- 10 across the whole sample area causing the zinc surface to become passive. In the absence of Ge a pH gradient is established with respect to anodic and cathodic sites with only cathodic areas reaching a pH of 9 - 10.

- In ZAM-1.8 Ge samples, this passivation delays the initiation of localised corrosion by 6 – 15 hours. The delay in the intitaion of corrosion in the 1.8 wt. % Ge eutectic was dependent upon Mg_2Ge crystal surface area coverage and distribution. Once initiated, corrosion of the eutectic is somewhat constrained compared to that observed in the absence of Ge additions.

The findings of this work highlight the potential use of Ge to form thermally and mechanically stable, intermetallic ‘smart release’ capsules which can be incorporated into metallic coatings.

Authors

N. Wint: Validation, formal analysis, investigation, data curation, writing-original & draft, writing- review and editing.
A. D. Malla investigation, data curation

N. Cooze investigation, data curation

T. Savill investigation, data curation

S. Mehraban investigation, data curation, methodology

T. Dunlop investigation, data curation

J. H. Sullivan Conceptualization, methodology, Validation, formal analysis, investigation, data curation, writing-original & draft, writing- review and editing.

D. Penney Conceptualization, methodology, validation, formal analysis, investigation

G.Williams: Conceptualization, methodology, writing- review and editing, supervision
H.N. McMurray: Conceptualization, methodology, writing- review and editing, supervision

Declaration of interests

The authors declare that they have no known competing financial interests or personal relationships that could have appeared to influence the work reported in this paper.

6. Acknowledgments

The authors would like to thank Tata Steel UK and EPSRC for funding via the COATED2 Centre for Doctoral Training (EP/L015099/1).

The authors would like to acknowledge the financial support of the RFCS (Research Fund for Coal and Steel, grant number: RFSR-CT-2015-00011) support and all the partners: ArceloMittal (France), OCAS (Belgium), Max Planck Institut (Germany), Tata steel (Netherlands), Voestalpine (Austria) for the supply of samples; Chimie ParisTech (France), University of Chemistry and Technology in Prague (Czech Republic) and Dominique

Thierry and Nathalie LeBozec of Institut de la Corrosion, France for coordinating the project.

The raw/processed data required to reproduce these findings cannot be shared at this time as the data also forms part of an ongoing study.

7. References

1. P. Volovitch, C. Allely, K. Ogle, Understanding corrosion via corrosion product characterization: i. Case study of the role of Mg alloying in Zn-Mg coating on steel, Corrosion Science. 51, 1251-1262 (2009).

2. P. Volovitch, T. N. Vu, C. Allely, A. A. Aal, K. Ogle, Understanding corrosion via corrosion product characterization: II. Role of alloying elements in improving the corrosion resistance of Zn–Al–Mg coatings on steel, Corrosion Science. **53**, 2437-2445 (2011).

3. X. Zhang, T. N. Vu, P. Volovitch, C. Leygraf, K. Ogle, I. Odnevall Wallinder, The initial release of zinc and aluminium from non-treated Galvalume and the formation of corrosion products in chloride containing media, Applied Surface Science. **258**, 4351-4359 (2012).

4. J. Sullivan, N. Cooze, C. Gallagher, T. Lewis, T. Prosek, D. Thierry, *In situ* monitoring of corrosion mechanisms and phosphate inhibitor surface deposition during corrosion of zinc–magnesium–aluminium (ZAM) alloys using novel time-lapse microscopy, Faraday Discussions. **180**, 361-379 (2015).

5. J. Duchoslav, M. Arndt, R. Steinberger, T. Keppert, G. Luckeneder, K.H. Stellnberger, J. Hagler, C.K. Riener, G. Angeli, D. Stifter, Nanoscopic view on the initial stages of corrosion of hot dip galvanized Zn–Mg–Al coatings, Corrosion Science. **83**, 327-334 (2014).

6. T.N. Vu, P. Volovitch, K. Ogle, The effect of pH on the selective dissolution of Zn and Al from Zn–Al coatings on steel, Corrosion Science. **67**, 42-29 (2013).

7. M. Salgueiro Azevedo, C. Allely, K. Ogle, P. Volovitch, Corrosion mechanisms of Zn(Mg,Al) coated steel: 2. The effect of Mg and Al alloying on the formation and properties of corrosion products in different electrolytes, Corrosion Science. **90**, 482-490 (2015).

8. T. Prosek, D. Persson, J. Stoulil, D. Thierry, Composition of corrosion products formed on Zn–Mg, Zn–Al and Zn–Al–Mg coatings in model atmospheric conditions, Corrosion Science. **86**, 231-238 (2014).

9. J.D. Yoo, P. Volovitch, A.A. Aal, C. Allely, K. Ogle, The effect of an artificially synthesized simonkolleite layer on the corrosion of electrogalvanized steel, Corrosion Science. **70**, 1-10 (2013).

10. P. Volovitch, M. Serdechnova, K. Ogle, Aqueous Corrosion of Mg-Al Binary Alloys: Roles of Al and Mg, Corrosion. **68**, 557-570 (2012).

11. T. Lostak, A. Maljusch, B. Klink, S. Krebs, M. Kimpel, J. Flock, S. Schulz, W. Schuhmann, Zr-based conversion layer on Zn-Al-Mg alloy coated steel sheets: insights into the formation mechanism, Electrochimica Acta. **137**, 65-74 (2014).

12. R. Hausbrand, M. Stratmann, M. Rohwerder, Corrosion of zinc–magnesium coatings: Mechanism of paint delamination, Corrosion Science. **51**, 2107-2114 (2009).

13. B. Schuhmacher, C. Schwerdt, U. Seyfert, O. Zimmer, Innovative steel strip coatings by means of PVD in a continuous pilot line: process technology and coating development, Surface and Coatings Technology. **163**, 703-709 (2003).

14. J.L. Davies, C.F. Glover, J. Van de Langkruis, E. Zoestbergen, G. Williams, The effect of Mg concentration on the resistance of PVD Zn-Mg coatings to corrosion driven organic coating delamination, Corrosion Science. **100**, 607-618 (2015).

15. J. Duchoslav, M. Arndt, T. Keppert, G. Luckeneder, D. Stifter, XPS investigation on the surface chemistry of corrosion products on ZnMgAl-coated steel, Analytical and Bioanalytical Chemistry. **405**, 7133-7144 (2013).

16. S. Schuerz, M. Fleischanderl, G. H. Luckeneder, K. Preis, T. Haunschmied, G. Mori, A.C. Kneissl, Corrosion behaviour of Zn–Al–Mg coated steel sheet in sodium chloride-containing environment, Corrosion Science. **51,** 2355-2363 (2009).

17. T. Prosek, N. Larche, M. Vlot, F. Goodwin, D. Thierry, Corrosion performance of Zn–Al–Mg coatings in open and confined zones in conditions simulating automotive applications, Materials and Corrosion. **61**, 412-420 (2010).

18. L. Jiang, M. Wolpers, P. Volovitch, K. Ogle, Activation and inhibition of Zn–Al and Zn–Al–Mg coatings on steel by nitrate in phosphoric acid solution, Corrosion Science. **60**, 256-264 (2012).

19. J.H. Sullivan, S. Mehraban, J. Elvins, In situ monitoring of the microstructural corrosion mechanisms of zinc–magnesium–aluminium alloys using time lapse microscopy, Corrosion Science. **53**, 2208-2215 (2011).

20. J. Elvins, J. A. Spittle, D. A. Worsley, Microstructural changes in zinc aluminium alloy galvanising as a function of processing parameters and their influence on corrosion, Corrosion Science. **47**, 2740-2759 (2005).

21. J. Elvins, J.A Spittle, J.H. Sullivan, D.A. Worsley, The effect of magnesium additions on the microstructure and cut edge corrosion resistance of zinc aluminium alloy galvanised steel, Corrosion Science. **50**, 1650-1658 (2008).

22. T. Prosek, A. Nazarov, U. Bexell, D. Thierry, J. Serak, Corrosion mechanism of model zinc–magnesium alloys in atmospheric conditions, Corrosion Science. **50**, 2216-2231 (2008).

23. N. LeBozec, D. Thierry, A. Peltola, L. Luxem, G. Luckeneder, G. Marchiaro, M. Rohwerder. Corrosion performance of Zn–Mg–Al coated steel in accelerated corrosion tests used in the automotive industry and field exposures. Materials and Corrosion. 64, 969-978 (2013).

24. N. LeBozec, D. Thierry, M. Rohwerder, D. Persson, G. Luckeneder, L. Luxem. Effect of carbon dioxide on the atmospheric corrosion of Zn–Mg–Al coated steel. Corrosion Science. 74, 379-386 (2013).

25. D. Crespy, K. Landfester, J. Fickert, M. Rohwerder, *Self-Healing for Anticorrosion Based on Encapsulated Healing Agents*. In: Hager M., van der Zwaag S., Schubert U. (eds) Self-healing Materials. Advances in Polymer Science, vol 273. (Springer, Cham, 2016).

26. D. Shchukin, H. Möhwald, Self-Repairing Coatings Containing Active Nanoreservoirs, Small, 3: 926-943 (2007).

27. J.-H. Huang, C-P. Liu, The introduction of magnesium and hydrogen introduction in sputtered zinc oxide thin films, Thin Solid Films. **498**, 152-157 (2006).

28. R.L. Liu, S. Thomas, J.R. Scully, G. Williams, N. Birbilis, An experimental survey of the cathodic activation of metals including Mg, Sc, Gd, La, Al, Sn, Pb and Ge in dilute chloride solutions of varying pH, Corrosion. **73**, 469–505 (2017).

29. R.L. Liu, Z.R. Zeng, J.R. Scully, G. Williams, N. Birbilis, Simultaneously improving the corrosion resistance and strength of magnesium via low levels of Zn and Ge additions, Corrosion Science. **140**, 18-29 (2018).

30. R. L. Liu, M. F. Hurley, A. Kvryan, G. Williams, J. R. Scully, N. Birbilis, Controlling the corrosion and cathodic activation of magnesium via microalloying additions of Ge, Scientific Reports. **6**, 28747 (2016).

31. S.Gh.R. Emad, X. Zhou, S. Morsch, S.B. Lyon, Y. Liu, D. Graham, S.R. Gibbon. How pigment volume concentration (PVC) and particle connectivity affect leaching of corrosion inhibitive species from coatings. Progress in Organic Coatings, 134, 360-372 (2019).

32. M. Garcia-Heras, A. Jimenez-Morales, B. Casal, J.C. Galvan, S. Radzki, M. A. Villegas, Preparation and electrochemical study of cerium-silica sol–gel thin films, Journal of Alloys and Compounds. **380**, 219–224 (2004).

33. M.F. Montemor, Functional and smart coatings for corrosion protection: a review of recent advances, Surface and Coatings Technology. **258**, 17-37 (2014).

34. A.J. Vreugdenhil, M.E. Woods, Triggered release of molecular additives from epoxy-amino sol–gel coatings, Progress in Organic Coatings. **53**, 119-125 (2005).

35. D.G. Shchukin, H. Mohwald, Self-repairing coatings containing active nanoreservoirs, Small. **3,** 926–943 (2007).

36. D. Raps, T. Hack, J. Wehr, M.L. Zheludkevich, A.C. Bastos, M.G.S. Ferreira, O.Nuyken, Electrochemical study of inhibitor-containing organic-inorganic hybrid coatings on AA2024, Corrosion Science. **51**, 1012–1021 (2009).

37. F. Maia, J. Tedim, A. D. Lisenkov, A. N. Salak, M. L. Zheludkevich, M. G. Ferreira, Silica nanocontainers for active corrosion protection, Nanoscale. **4**, 1287–1298 (2012).

38. T. H. Tran, A. Vimalanandan, G. Genchev, J. Fickert, K. Landfester, D. Crespy, M. Rohwerder, Regenerative nano-hybrid coating tailored for autonomous corrosion protection, Advanced Materials. **27**, 3825–3830 92015).

39. S.R. White, N.R. Sottos, P.H. Geubelle, J.S. Moore, M.R. Kessler, S.R. Sriram, E. N. Brown, S. Viswanathan, Autonomic healing of polymer composites, Nature. **409,** 794–797 (2001).

40. E. Shchukinaa, D. Shchukina, D. Grigoriev, Effect of inhibitor-loaded halloysites and mesoporous silica nanocontainers on corrosion protection of powder coatings, Progress in Organic Coatings. **102**, 60-65 (2017).

41. D. Fix, D.V. Andreeva, D.G. Shchukin, Y.M. Lvov, H. Möhwald, Application of inhibitor-loaded halloysite nanotubes in active anti-corrosive coatings, Advanced Functional Materials. **19**, 1720–1727 (2009).

42. M. Sun, A. Yerokhin, M. Ya. Bychkova, D. V. Shtansky, E. A., Levashov, A. Matthews, Self-healing plasma electrolytic oxidation coatings doped with benzotriazole loaded halloysite nanotubes on AM50 magnesium alloy. Corrosion Science. **111**, 753–769 (2016).

43. A.M. Pavlov, S.A. Gabriel, G.B. Sukhorukov, D.J. Gould, Improved and targeted delivery of bioactive molecules to cells with magnetic layer-by-layer assembled microcapsules. Nanoscale. **7**, 9686–9693 (2015).

44. J. Tedim, M. L. Zheludkevich, A. C. Bastos, A. N. Salak, A. D. Lisenkov, M. G. S. Ferreira, Influence of preparation conditions of layered double hydroxide conversion films on corrosion protection, Electrochimica Acta. **117**, 164-171 (2014).

45. G. Williams, S. Geary, H.N. McMurray, Smart release corrosion inhibitor pigments based on organic ion-exchange resins, Corrosion Science. **57**, 139–147 (2012).

46. B. D. Mert, B. Yazici, S. B. Lyon, Electrochemical synthesis of novel conductive polymer and corrosion protection properties on aluminium, Corrosion Engineering and Science Technology. **48**, 506-512 (2013).

47. T. R. Khan, A. Vimalanandan, F. Marlow, A. Andreas, M. Rohwerder, Electro-codeposition of Modified Silica Colloids and Copper. Zeitschrift für Physikalische Chemie. **227**, 1083-1095 (2013).

48. M. Azizi, W. Schneider, W. Plieth, Electrolytic co-deposition of silicate and mica particles with zinc, Journal of Solid State Electrochemistry. **9**, 429-437 (2005).

49. A. Bund, D. J. Thiemig, Influence of bath composition and pH on the electrocodeposition of alumina nanoparticles and copper, Journal of Applied Electrochemistry. **37**, 345-351 (2007).

50. D. Aslanidis, J. Fransaer, J.-P. Celis, The Electrolytic Codeposition of Silica and Titania Modified Silica with Zinc, *Journal of the Electrochemical Society*. **144**, 2352-2357 (1997).

51. J. Fransaer, E. Leunis, T. Hirato, J.-P. Celis, Aluminium composite coatings containing micrometre and nanometre-sized particles electroplated from a non-aqueous electrolyte, Journal of Applied Electrochemistry. **32**, 123-128 (2002).

52. I. Zhitomirsky, Cathodic electrodeposition of ceramic and organoceramic materials. Fundamental aspects, Advances in Colloid and Interface Science. **32**, 123-128 (2002).

53. J. Lyklema, *Fundamentals of Interface and Colloid Science Vol II* (London: Academic, 2001).

54. Z. Xie, S. Shan, Nanocontainers-enhanced self-healing Ni coating for corrosion protection of Mg alloy, Journal of Materials Science. **53** (2017)

55. D. Borisova, H. Mohwald, D.G. Shchukin, Influence of embedded nanocontainers on the efficiency of active anticorrosive coatings for aluminum alloys part I: influence of nanocontainer concentration, ACS Applied Materials and Interfaces. **4**, 2931-2939 (2012).

56. T. R. Khan, A. Erbe, M. Auinger, F. Marlow, M. Rohwerder, Electrodeposition of zinc–silica composite coatings: challenges in incorporating functionalized silica particles into a zinc matrix, Science and Technology of Advanced Materials. **12**, 055005 (2011).

57. E. Joussein, S. Petit, J. Churchman, B. Theng, D. Righi, B. Delvaux, Halloysite clay minerals—a review, Clays and Clay Minerals. **40**, 383-426 (1992).

58. S. Mehraban, J. Malone, N. Lavery, J. Sullivan, D. Penney, S. Brown, Increased Corrosion Resistance of Zinc Magnesium Aluminum Galvanised Coating through Germanium Additions, *ECS Trans.* **75**, 1-15 (2017).

59. P.C. Dodds, G. Williams, J. Radcliffe, Chromate-free smart release corrosion inhibitive pigments containing cations, Progress in Organic Coatings. **102**, 107-114 (2017).

60. G. Williams, H. N. McMurray, Inhibition of corrosion driven delamination on iron by smart-release bentonite cation-exchange pigments studied using a scanning Kelvin probe technique, Progress in Organic Coatings. **102**, 18-28 (2017).

61. G. Williams, H. N. McMurray, M. Loveridge, Inhibition of corrosion-driven organic coating disbondment on galvanised steel by smart release group II and Zn(II)-exchanged bentonite pigments, Electrochimica Acta. **55**, 1740-1748 (2010).

62. G. Williams, H. N. McMurray, Journal of the Electrochemical Society, **155**, C340 (2008).

63. S. Bohm, H.N. McMurray, S.M. Powell, D.A. Worsley, Electrochimica Acta. **45**, 2165 (2000).

64. D. Worsley, H. N. McMurray, A. Belghazi, Chemical Commununications. 2369 (1997).

65. S. M. Powell, D. A. Worsley, British Corrosion Journal. **36**, 42 (2001).

66. H. S. Isaacs, Journal of the Electrochemical Society. **183**, 722 (1991).

67. A. C. Bastos, M. C. Quevedo, O. V. Karavai, M. G. S. Ferreira, Journal of The Electrochemical Society. **164**, C973 (2017).

68. G.W.C. Kaye, T.H. Laby, *Tables of Physical and Chemical Constants*, p. 219, Longman, London (1986).

69. G. Williams, H. N. McMurray, Corrosion. **62**, 231 (2006).

70. G. Williams, H. N. McMurray, R. Grace, Electrochimica Acta. **55**, 7824 (2010).

71. D.A. Worsley, H.N. McMurray, J.H. Sullivan, I.P. Williams, Corrosion. **60**, 437 (2004).

72. A.C. Bastos, M.L. Zheludkevich, M.G.S. Ferreira, Portugaliae Electrochimica Acta. **26**, 47 (2008).

73. A. Leng, H. Streckel, M. Stratmann**,** Corrosion Science. **41**, 547 (1999).

74. P. Schmutz, G. Frankel, Journal of the Electrochemical Society.**145**, 2285 (1998).

75. M. Rohwerder, F. Turcu, High-resolution Kelvin probe microscopy in corrosion science: Scanning Kelvin probe force microscopy (SKPFM) versus classical scanning Kelvin probe (SKP). Electrochimica Acta. 53, 290 (2007).

76. M. Iannuzzi, K.L. Vasanth, G.S. Frankel. Unusual Correlation between SKPFM and Corrosion of Nickel Aluminum Bronzes. Journal of The Electrochemical Society, 164, C488 (2017).

77. N. Wint, N. Cooze, J. R. Searle, J. H. Sullivan, G. Williams, H. N. McMurray, G. Luckeneder, C. Riener. Journal of the Electrochemical Society. 166, C3147 (2019).

78. L.G. Sillen, A.E. Martell, Stability Constants of Metal-Ion Complexes, The Chemical Society, London (1964)

79. C. F. Baes, R. E. Mesmer, The Hydrolysis of Cations, Wiley, New York (1976).

Figure 1. SEM image showing the surface of industrial ZAM- 0 Ge alloy.

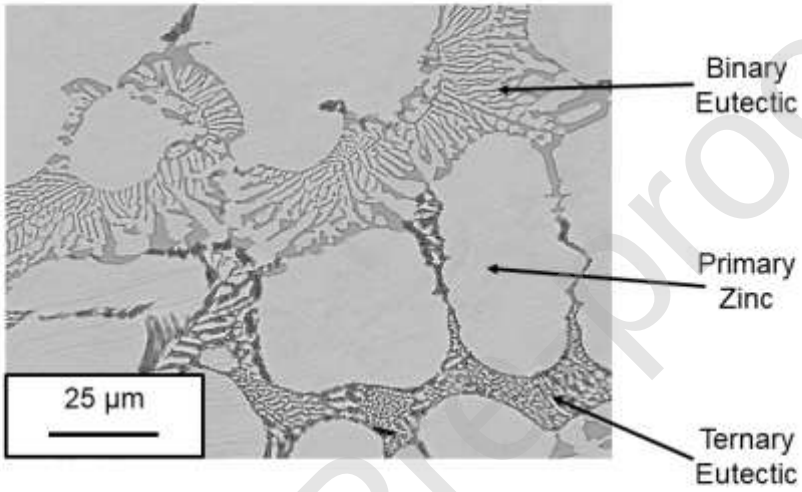

Figure 2. SEM images showing the surface of. a) ZAM-0 Ge, b.) ZAM-0.19 Ge, c.) ZAM-0.87 Ge and d) ZAM-1.8 Ge.

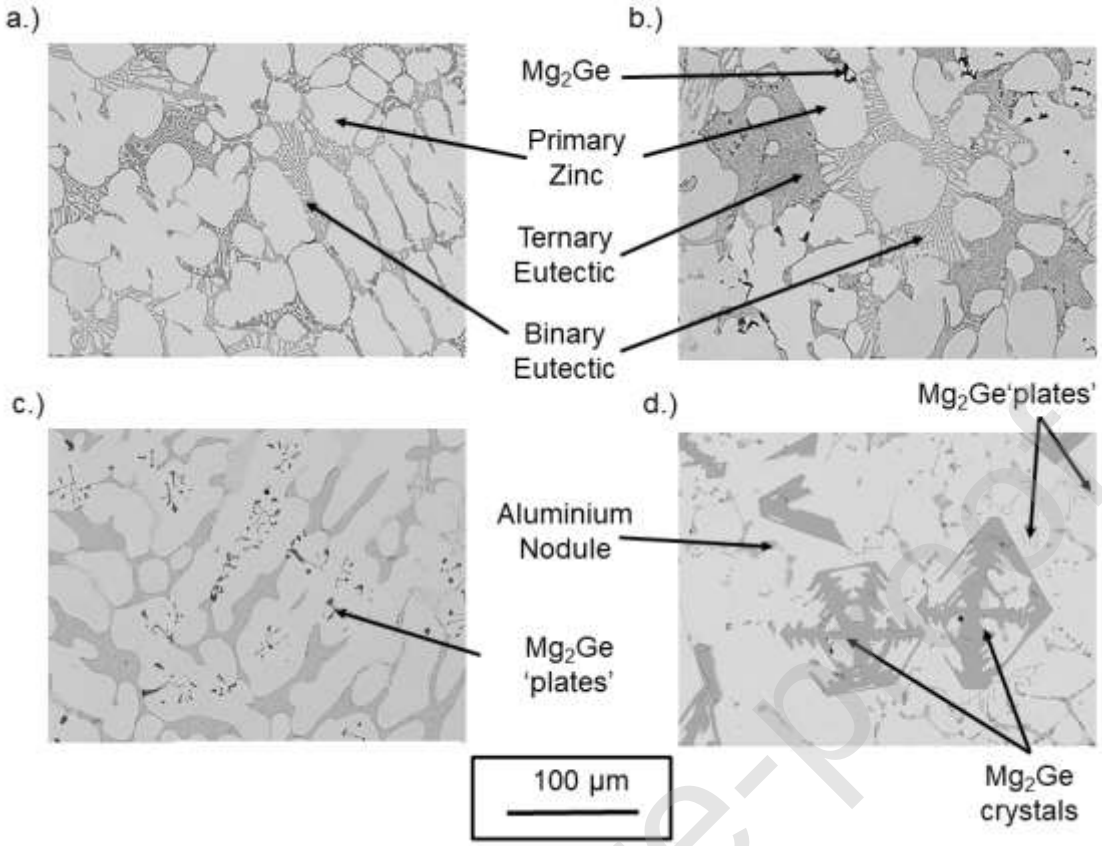

Figure 3. XRD analysis ZAM-0.87 Ge alloy

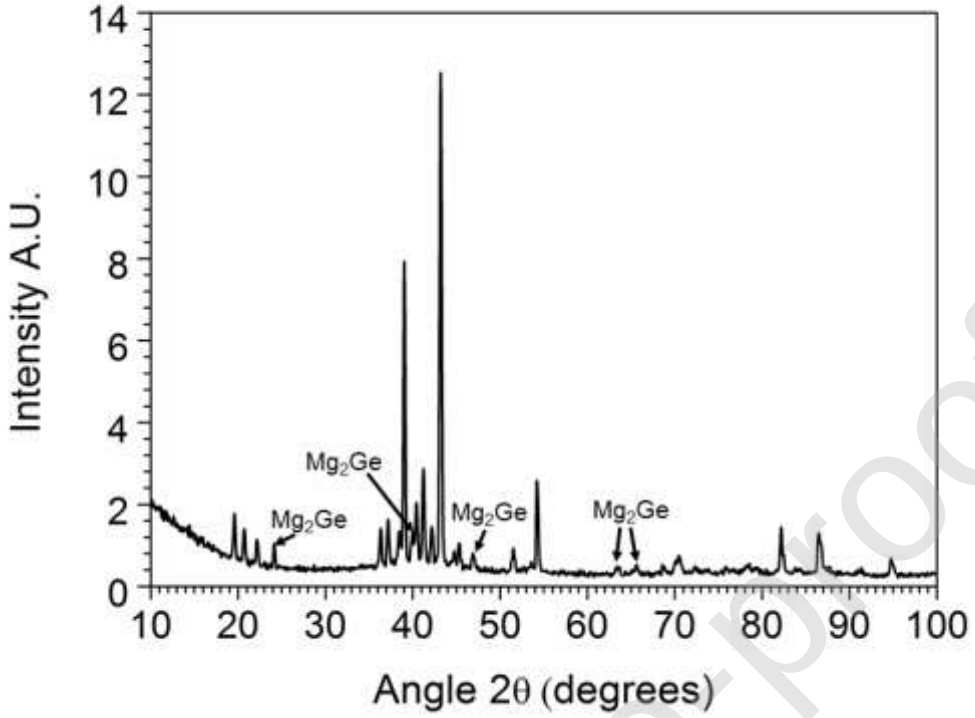

Figure 4. The time dependent open circuit potential (OCP) of various ZAM-Ge immersed in 0.17 M NaCl at pH 7.

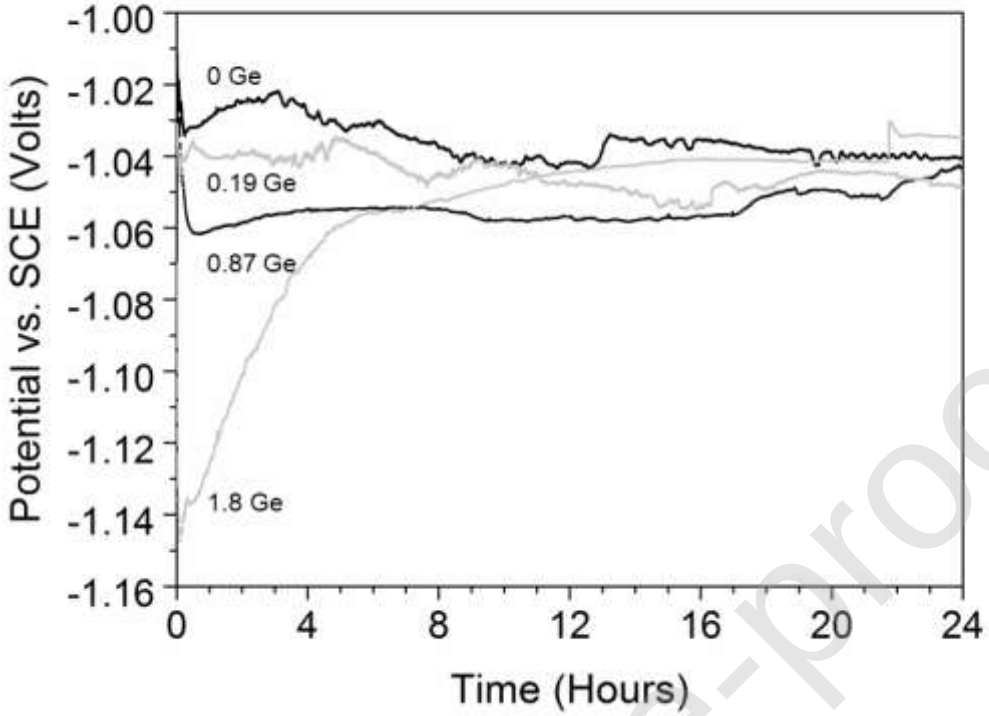

Figure 5. The Volta potential difference maps of an area of ZAM-0.8 7Ge.

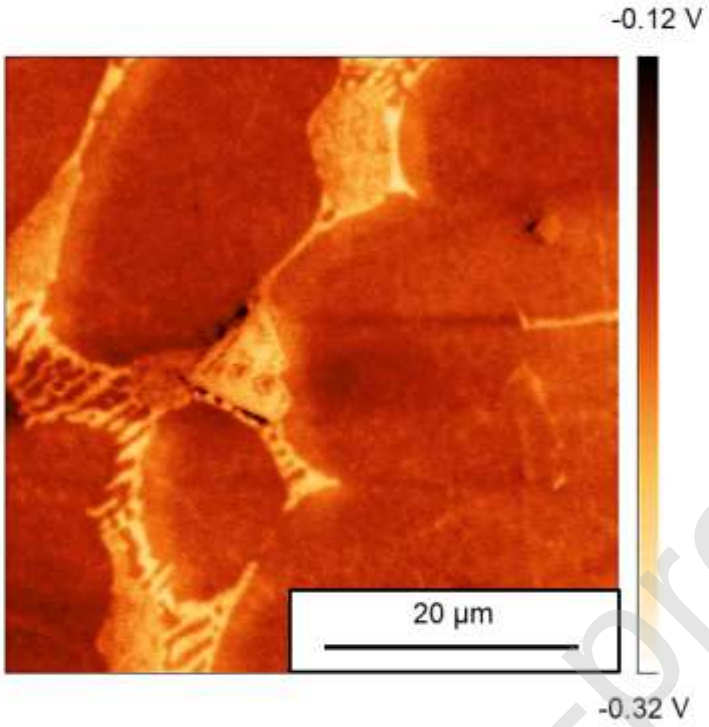

Figure 6. SVET false colour maps showing normal current density measured above ZAM-Ge alloys immersed in pH 7 0.17 mol.dm^{-3} NaCl for 24 hours.

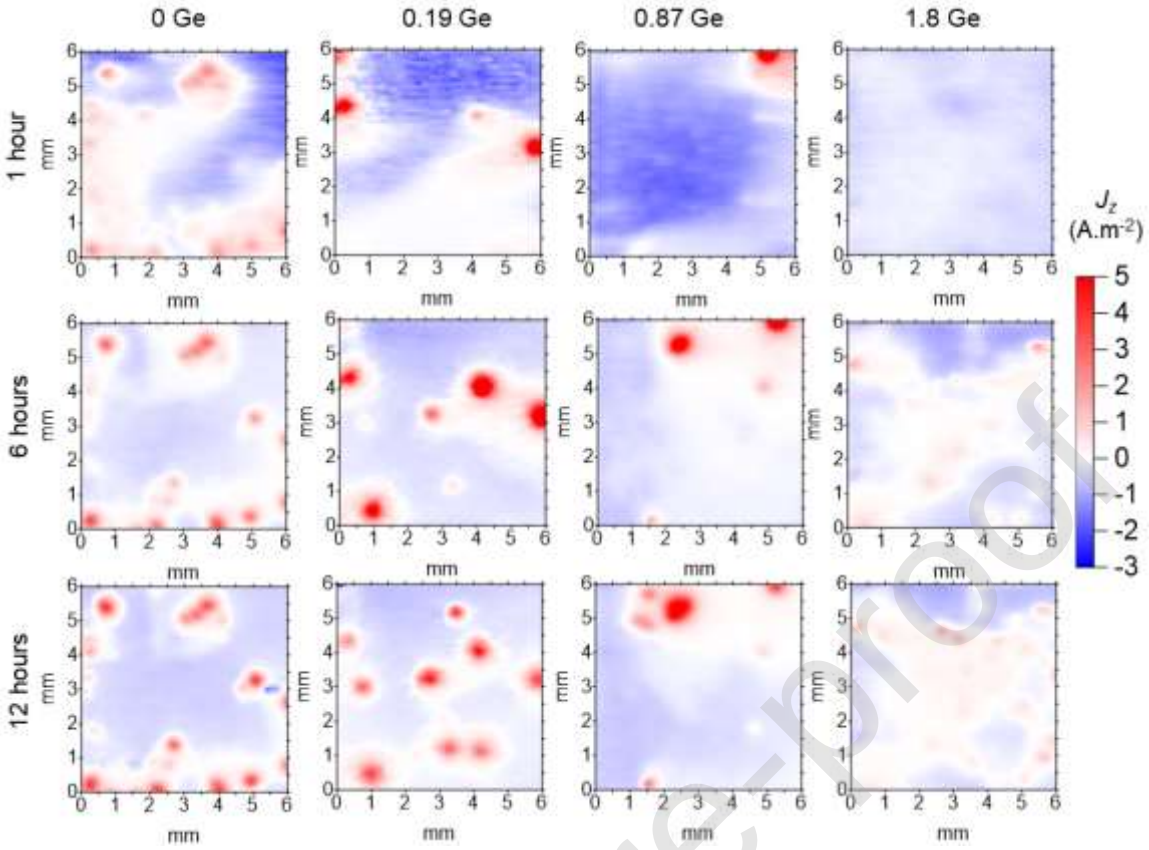

Figure 7. Optical microscope images of the a.) ZAM-0 Ge and b.) ZAM-1.8 Ge surface taken in situ under immersion conditions in pH 7 0.17 mol.dm^{-3} NaCl solution.

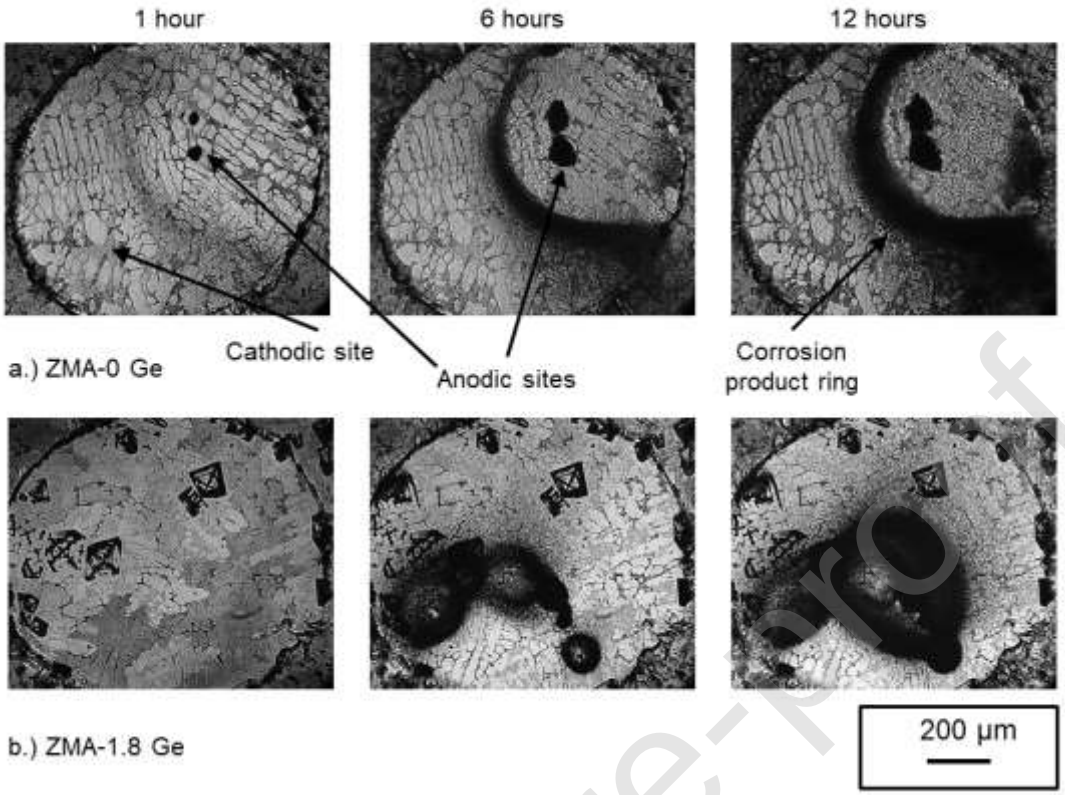

Figure 8. Optical microscopy images of 3 different areas of the ZAM-1.8Ge alloy surface after various times of immersion in pH 7 0.17 mol.dm^{-3} NaCl.

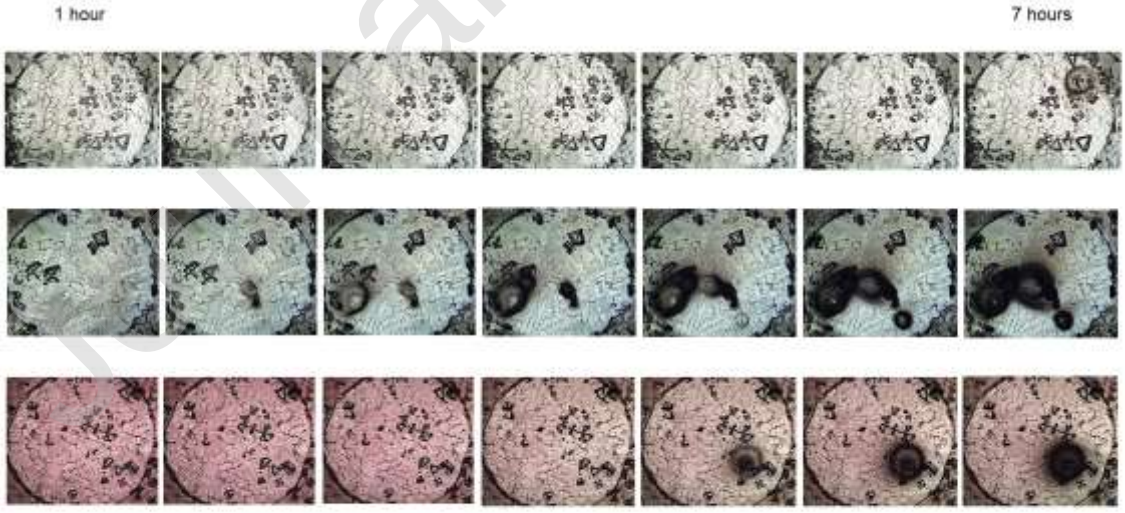

Figure 9. SEM image of the ZAM-1.8 Ge surface with EDS analysis of an individual Mg_2Ge crystal obtained a.) prior to and b.) after 2 hours of immersion in pH 7 0.17 mol.dm^{-3} NaCl.

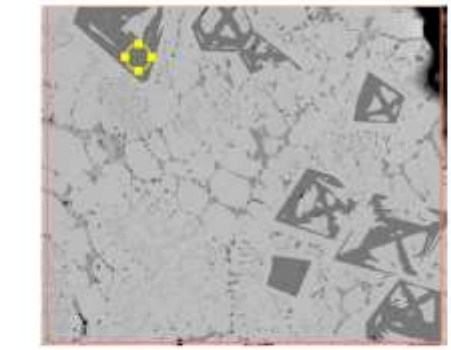

a.)

Element	Norm. C (wt. %)
Germanium	52.98
Magnesium	40.92
Zinc	6.09
Aluminium	0

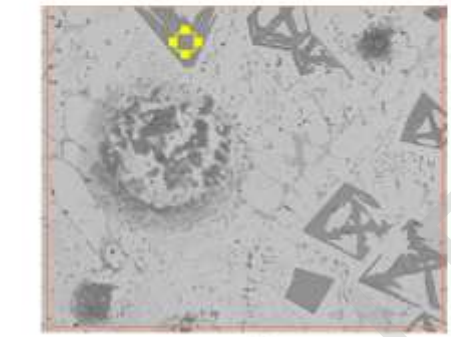

b.)

Element	Norm. C (wt. %)
Germanium	61.90
Magnesium	20.91
Zinc	16.88
Aluminium	0.31

Figure 10. Optical microscope image of the ZAM- 0 Ge surface taken after 4 minutes of immersion in pH 7 0.17 mol.dm^{-3} NaCl solution in the presence of phenolphthalein indicator.

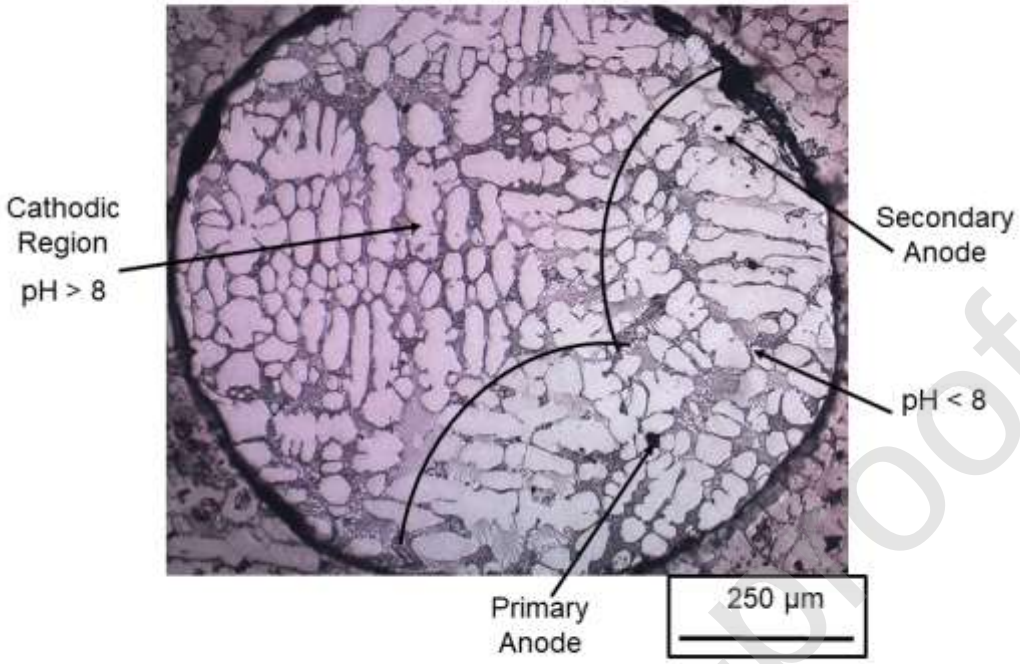

Figure 11. Optical microscopy images of the ZAM-1.8 Ge after a.) 2 minutes, b.) 4 minutes, c.) 1 hour and d.) 14 hours of immersion in pH 7 0.17 mol.dm^{-3} NaCl solution.

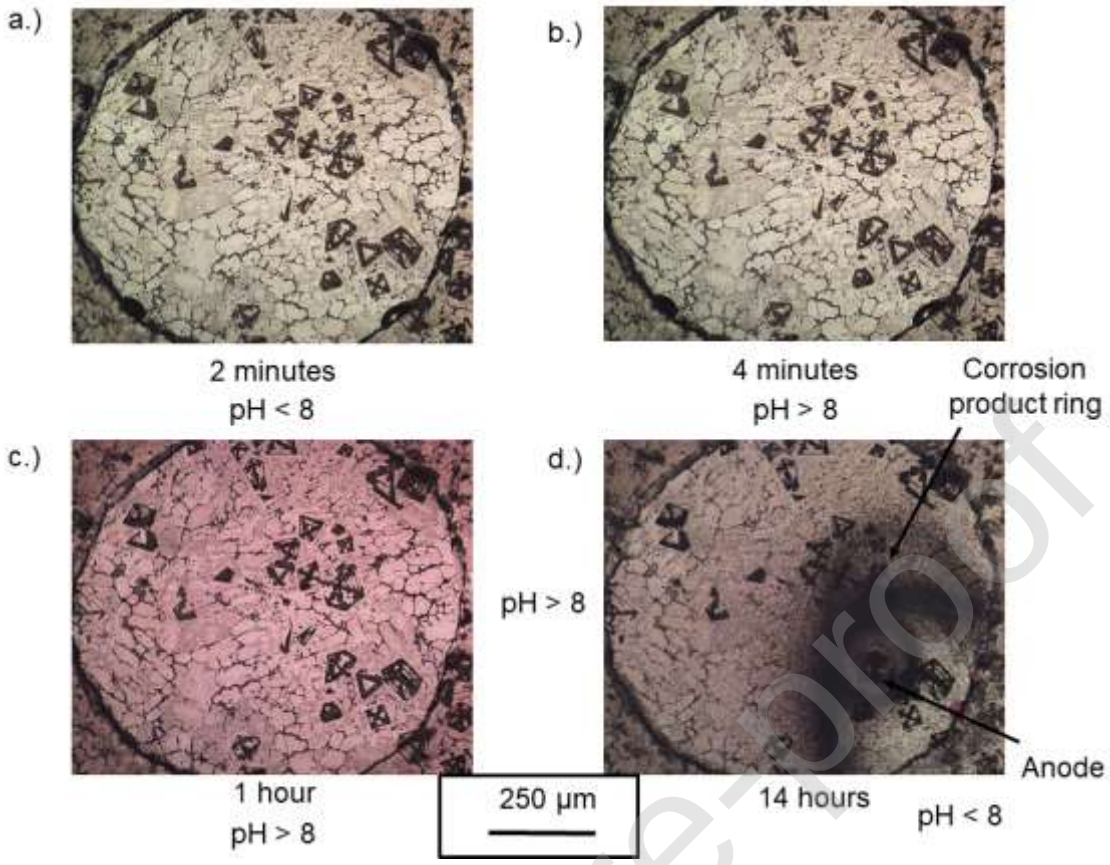

Figure 12. A photo of universal indicator paper which had been applied to a droplet of 0.17 mol.dm^{-3} NaCl at pH 7 applied to ZAM-0 Ge for 1 hour.

Figure 13. SVET measured time dependent total anodic current (*I(t)*) due to localised corrosion for ZAM-0 Ge and ZAM 1.8 Ge. The ranges represent the maximum and minimum currents measured at each hour over three experiments for each material.

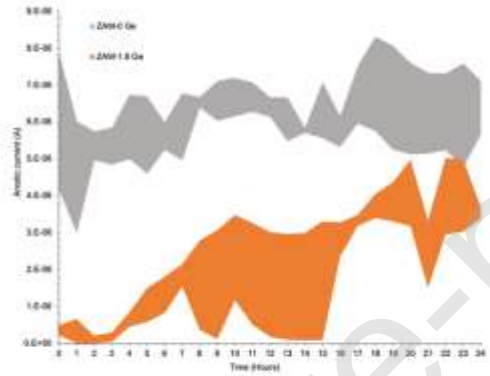

8. Tables

Table 1. Zn-Mg-Al-Ge (ZAM-Ge) alloy compositions

Sample	Zn (wt. %)	Mg (wt. %)	Al (wt. %)	Ge (wt. %)
ZAM-0 Ge	96.80	1.60	1.60	0.00
ZAM-0.19 Ge	96.61	1.59	1.59	0.19
ZAM-0.87 Ge	95.96	1.58	1.58	0.87
ZAM-1.8 Ge	95.08	1.57	1.57	1.80

Table 2: Area fraction of phases present in ZAM-Ge samples

Sample	Primary Zn (surface area %)	Eutectic (surface area %)	Mg_2Ge (surface area %)
ZAM-0 Ge	67 ± 2	32 ± 2	0
ZAM-0.19 Ge	70 ± 6	29 ± 6	2 ± 1
ZAM-0.87 Ge	75 ± 1	22 ± 1	3 ± 1
ZAM-1.8 Ge	78 ± 6	7 ± 1	14 ± 7

Table 3: Composition of phases present within ZAM-Ge samples obtained using EDS.

Sample	Zn (wt.%)	Mg (wt.%)	Al (wt.%)	Ge (wt.%)
	Industrial ZAM-0Ge			
Primary zinc	99.49 ± 3.0	0.04 ± 0.0	0.47 ± 0.0	/
Binary Eutectic	94.64 ± 2.4	3.55 ± 0.2	1.81 ± 0.1	/
Ternary Eutectic	89.59 ± 2.7	3.34 ± 0.2	7.08 ± 0.3	/
	ZAM -0Ge			
Primary zinc	99.36 ± 3.3	/	0.64 ± 0.1	/
Binary Eutectic	95.2 ± 2.4	2.73 ± 0.2	2.07 ± 0.1	/
Ternary Eutectic	88.54 ± 2.5	0.41 ± 0.0	11.05 ± 0.5	/
	ZAM - 0.19 Ge			
Primary zinc	99.96 ± 3.4	/	0.04 ± 0.0	/
Binary Eutectic	94.11 ± 2.8	5.01 ± 0.3	0.87 ± 0.1	/
Ternary Eutectic	88.24 ± 5.7	1.91 ± 0.1	8.94 ± 0.4	0.91 ± 0.1
	ZAM - 0.87 Ge			
Primary zinc	99.18 ± 2.9	/	0.82 ± 0.1	/
Binary Eutectic	95.79 ± 3.5	2.15 ± 0.2	1.75 ± 0.1	0.32 ± 0.0

Ternary Eutectic	86.85 ± 1.9	1.74 ± 0.1	11.41 ± 0.4	/
	ZAM – 1.8 Ge			
Primary zinc	99.99 ± 2.8	/	/	/
Eutectic	85.16 ± 4.9	1.77 ± 0.1	11.58 ± 0.5	1.49 ± 0.1

Table 4: Linear polarisation resistance measurements obtained for ZAM-0 Ge and ZAM-1.8 Ge where the samples were polarised by 15 mV at a scan rate of 0.166 mVs^{-1} in 0.17 $mol.dm^{-3}$ NaCl pH 7.

	Polarisation resistance (R_p) Ω cm^{-2}	
Time	ZAM – 0 Ge	ZAM – 1.8 Ge
10 minutes	846	11380
1 hour	1382	9842
2 hours	1086	11697
3 hours	1045	11155
4 hours	1016	11353
5 hours	847	13781

Table 5: SVET derived metal loss from ZAM-Ge samples after immersion in pH 7 0.17 M NaCl for 24 hours.

Sample	**Mass Loss ($g.m^{-2}$)**
ZAM-0 Ge	5.01 ± 0.49
ZAM-0.19 Ge	8.53 ± 2.16
ZAM-0.87 Ge	4.41 ± 0.51
ZAM-1.80 Ge	2.11 ± 0.84